Combination of Filament-Heating and Cavity-Driven Circuit With Gain-Frequency Regulation Control for Magnetrons

Tsong-Shing Lee, *Member, IEEE*, Shyh-Jier Huang, *Senior Member, IEEE*, Yu-Ren Lin, Te-Chun Hung, *Member, IEEE*, and Chien-Chang Chen, *Member, IEEE*

***Abstract*—This article proposes the combination of filament-heating and cavity-driven circuit with gain-frequency regulation control for magnetrons. This article is motivated because some existent magnetron-driven systems often adopted two resonant circuits individually for filament heating and cavity driving, resulting in limited flexibility of power delivery and modulation. Therefore, this article develops an integrated resonant power circuit that excels at the capability improvement of filament heating and cavity driving in the same time such that the design process and power conversion can be simplified while the output power is effectively induced. Meanwhile, by considering that the microwave source emission in the magnetron is often affected by the variation of internal impedance, this article includes a gain-frequency tracking control. Through this way of controller design, both heating power and cavity power are found to be well regulated and the constant-power operation can be better achieved. To confirm the effectiveness of this magnetron-driven design, both circuit simulation and hardware realization are accomplished. Analysis results and experimental outcome support the practicality of the approach, benefiting the realization of microwave energy applications.**

***Index Terms*—Frequency regulation, integrated resonant circuit, magnetron.**

I. Introduction

MICROWAVE energy technology is increasingly applied to industry applications that include healthcare electronics, material surface coating, and thin-film material processing [1]. Magnetron is a high-power microwave output device that induces the electromagnetic field through filament heating and cavity driving. The control and operation of the magnetron is known to relate with the resonant structure of cavity and filament heater [2]. The rise in the operating temperature of magnetron caused changes in the internal equivalent impedance as well as unstable output microwaves, leading to an uneven power distribution on the load-bearing surface.

To solve this problem, a study based on the frequency stabilization in the microwave generation was investigated [3], [4], and the phase measurements for the improvement of planar magnetron were subsequently made [5]. These studies indicate that the comprehension of resonant behavior and filament-heating current is crucial to the development of a magnetron-driven system with stable microwave output.

Most magnetrons are operated with filament heating and cavity driving at the same time. This way of operation would lead to unnecessary heating when the magnetron is driven. The heating power is known to be alternating ac low voltage and large current, while the driving power is of dc high voltage so as to stimulate magnetron oscillations. Conventional design of driver circuit often utilized high-voltage transformer loop and filament feeder to individually supply the power for cavity driving and filament heating [6]. The class-E high-frequency resonant structure was employed to reach the close-loop control for magnetron drive [7]. The harmonic-tuning network with snubber circuit to reduce resonant voltage peak stress was meanwhile suggested [8], which was followed by the use of phase-locked loop or parallel operation to improve the microwave performance of magnetrons [9]–[11]. Later on, a method of using two sets of converters to reheat the filament and supply the driving voltage was made, and the burst-mode operation was used to adjust the microwave power [12]. The modified parallel resonance driving architecture [13], [14], the *LLC* resonant circuit [15]–[17], and the bridge converter with resonant tank were all suggested to boost the output voltage [18]–[20]. With the aid of dual resonant circuit and pulse frequency modulation, these circuit designs were proved capable of achieving high voltage gain [21]–[24]. Encouraging results of circuit design were gained from the aforementioned methods, yet each of them came with some demerits in certain respects, possibly restricting the scope of microwave energy application.

In this article, the design and realization of an integrated resonant system with gain-frequency regulation control for magnetron driving is proposed. This method consists of a simplified single-stage integrated circuit with heating and driving loop

Manuscript received February 25, 2020; revised June 3, 2020; accepted July 21, 2020. Date of publication July 27, 2020; date of current version September 22, 2020. Recommended for publication by Associate Editor R. Hui. *(Corresponding author: Shyh-Jier Huang.)*

Tsong-Shing Lee and Te-Chun Hung are with the Department of Electrical Engineering, Southern Taiwan University of Science and Technology, Tainan 71005, Taiwan (e-mail: tslee@stust.edu.tw; tchung@stust.edu.tw).

Shyh-Jier Huang is with the Department of Electrical Engineering, National Cheng Kung University, Tainan 70101, Taiwan (e-mail: clhuang@mail.ncku.edu.tw).

Yu-Ren Lin is with the MediaTek, Inc., Hsinchu 30078, Taiwan (e-mail: wl01663863 @gmail.com).

Chien-Chang Chen is with the Department of Automation Engineering, National Formosa University, Yunlin 632301, Taiwan (e-mail: nckufrank@gmail.com).

Color versions of one or more of the figures in this article are available online at https://ieeexplore.ieee.org.

Digital Object Identifier 10.1109/TPEL.2020.3012052

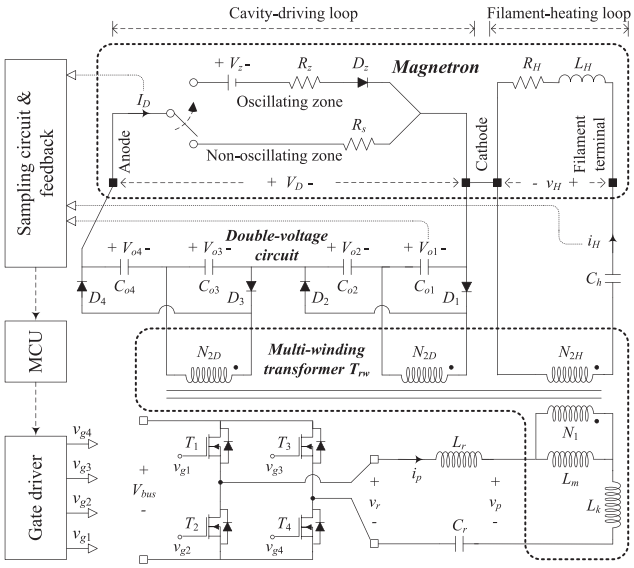

Fig. 1. Configuration of the proposed integrated magnetron-driven system.

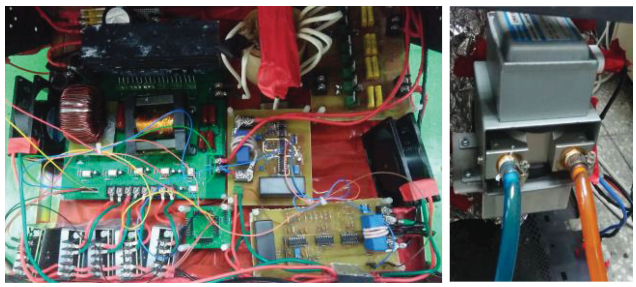

(Magnetron power supply system) (Magnetron cavity)

Fig. 2. Photograph of the prototype.

design, in which the load characteristics of cavity are concerned. Through this way of regulation, the constant-power control for stable operation of magnetron is reached and the consumption of unnecessary power loss is largely reduced. This regulation design is completed through the resonance gain analysis of frequency response of both heating circuit and driving circuit, by which the flexible pulse frequency modulation is applied to adjust the microwave output power when encountering any load variation. Both circuit simulation for parameter determination and hardware realization for performance evaluation are made. The features of the proposed method are listed as follows.

1) The method includes a gain-frequency regulation control, by which it ensures to realize the filament heating first, and then, the cavity driving one. With this flexible preheating power modulation mechanism, the driving power can be reduced.
2) This article proposes an integrated single-stage resonant power circuit with gain-frequency analysis and parameter calculation for two loops of filament-heating loop and cavity-driving one.
3) This article presents a systematic design procedure for the magnetron power system, which can be extended as a didactic tool to help practitioners become more acquainted with microwave energy applications.

In this article, Section II describes the configuration of the proposed magnetron system, Section III addresses the integrated circuit and its resonance gain analysis, Section IV illustrates the control strategies of regulation control, Section V gives the experimental results. Finally, Section VI draws the conclusions.

II. Proposed System Design

Fig. 1 illustrates the architecture of the proposed integrated power circuit for magnetron drive, which comprises a full-bridge inverter, double-voltage circuit, multiwinding transformer T_{rw}, and magnetron load. The magnetizing inductance L_m and the leakage inductance L_k as well as L_r and C_r form an *LLC* resonant tank. The secondary terminal (N_{2H} and N_{2D}) of the transformer is integrated with series resonance capacitor C_h and double-voltage circuit to form a filament-heating loop and cavity-driving loop, respectively. Through this design, the system provides the cathode with high-frequency filament-heating current i_H and the cavity anode with electrode-oscillating voltage V_D required for 2450 MHz microwave of the magnetron.

In the figure, the filament-heating loop is formed by the integration of secondary winding N_{2H} and C_h with equivalent inductance L_H and resistance R_H so as to perform the step-down ratio of high-frequency resonance transfer, thus exhibiting the low voltage of v_H and high current of i_H of heating power while reducing the cost of filament heater and minimizing the use of magnetic components. By considering that L_H is mainly from spiral leads and its value may vary between factory batches, it is important to either use the dc heating current i_H or reduce the variation of ac heating current i_H such that the noise affecting the cavity of magnetron can be better minimized [6]–[8], [11]. As for the cavity-driven loop, it consists of two sets of secondary winding N_{2D}, double-voltage circuit with four times voltage step-up ratio, and cavity equivalent load. This loop comes with the high dc low-ripple current received from voltage V_D in order to deliver the microwave energy of a magnetron device. While the *LLC* resonant tank and transformer T_{rw} are designed to provide the primary voltage v_p for magnetron-driven system, the heating loop and driving loop provide v_H (i_H) and V_D (I_D) for filament-heating and cavity-oscillating process, respectively. Following the filament heating operated at the heating frequency of f_{sH}, the system subsequently drives the magnetron cavity at the operation frequency of f_{sD}. This regulation control and operation further ensures the provision of low dc driving voltage of V_D to facilitate the driving during the filament heating as well as the arrangement of low current of i_H to maintain continuous electron emission during the cavity driving. By comparing with published articles where the preheating and driving are performed simultaneously with a higher instability [6], the proposed method is relatively stable with less power loss.

Fig. 2 shows the photograph of the completed power supply system for magnetron drive. In the hardware realization, the use of silicon carbide planar MOSFET (SCT2080KE, Rohm) is to take advantage of its high-voltage resistance, fast switching, large voltage rating, and low ON-resistance. A gate-driven

TABLE I
SPECIFICATIONS OF THE MAGNETRON DEVICE

Specifications	Symbols	Values
Threshold voltage	V_z	3.9 kV
Resistance of filament	R_H	0.3 Ω
Inductance of filament	L_H	5 μH
Resistance of non-oscillating state	R_s	2 MΩ
Resistance of oscillating state	R_z	40 Ω
Heating voltage of filament	$v_{H,rms}$	5~30 V_{rms}
Heating current of filament	$i_{H,rms}$	5~15 A_{rms}

TABLE II
SPECIFICATIONS OF THE DESIGNED TRANSFORMER

Specifications	Symbols	Values
Magnetizing inductance	L_m	1.04 mH
Leakage inductance	L_k	32 μH
Number of turns at primary side	N_1	55
Number of turns at secondary side	N_{2D}, N_{2H}	197, 18
Turn ratio of transformer	n_D, n_H	3.573, 0.103

photocoupler isolation circuit (TLP-350, Toshiba) is then adopted to convert the driving signals of v_{s1}–v_{s4} of 3.3 V to v_{g1}–v_{g4} of 15 V. In this system, an input dc voltage $V_{\rm bus}$ of 310 V from the power-factor-correction circuit is employed. Detailed descriptions are discussed in the following.

A. Magnetron Driving

On the upper side of Fig. 1, the equivalent circuit of magnetron load is observed. The tungsten wire between filament terminal and cathode is deemed equivalent to the connection between resistance R_H and inductance L_H. The resonant cavity between cathode and anode has oscillating and nonoscillating zones. When the magnetron is operated in the nonoscillating zone, it is equivalent to the resistance R_s. Only when i_H and V_D are sufficient to induce the microwave power, the magnetron enters the oscillating zone, where the cavity load of magnetron amounts to the connection of diode D_z, resistance R_z, and source voltage V_z, where the load exhibits negative impedance characteristics.

To activate this magnetron to produce the microwave energy, the proposed system first applies the alternating current i_H to preheat the filament electrode and emit thermal electrons. It is followed by the high dc low-ripple voltage V_D employed for the cavity driving. Once electrons receive sufficient energy, high-frequency oscillations will be generated in the cavity along with the production of microwave energy of 2450 MHz. Table I tabulates the parameters of this proposed system, where an industrial magnetron (2M410A, Panasonic) served as the microwave source. In the heating loop, the source voltage $v_{H,rms}$ is 5–30 V and the current $i_{H,rms}$ is 5–15 A. The cavity-driving loop of magnetron provides the voltage V_D of 4 kV that is larger than the threshold voltage V_z of 3.9 kV. The operating power P_D of magnetron cavity is almost 1 kW. These design values enable the magnetron cavity to operate in an oscillating zone.

B. Realization of Multiwinding Transformer

The high-frequency multiwinding transformer T_{rw} is realized in this article. The range of heating frequency f_{sH} and cavity-driving frequency f_{sD} are both concerned. Note that the inductances of L_m and L_k are operated with external resonant components of L_r, C_r, C_h as well as secondary winding of N_{2H} and N_{2D} so that voltage decrement in the filament heating and voltage increment in the cavity driving are individually reached [11]–[18]. In this circuit, the manganese–zinc ferrite material is used for the transformer core because it presents a high saturation flux density $B_{\rm sat}$, a high relative permeability μ_r, and low iron loss. The study in this article chooses Ferroxcube PC40 for the transformer core, and its saturation flux density $B_{\rm sat}$ is 510 mT. Care must be taken to ensure that ΔB is within the appropriate range since excessive ΔB would increase the loss of transformer core. Following the selection of safety margin of 0.5, ΔB is calculated to be 265 mT while the required area A_p of a transformer frame is calculated as

$$A_p = \frac{(P_H + P_D)\,(1 + 1/\eta) \cdot 10^4}{2 \cdot \Delta B \cdot f_{sD,\min} \cdot J \cdot k_u}. \tag{1}$$

Then, by substituting the winding coefficient k_u of 0.2 of transformer bobbin and the current density J of 4 A/mm^2 of the wire conductor into (1) along with the operating power P_D of 1 kW and the filament-heating power P_H of 0.1 kW, A_p is calculated to be 22.59 cm^2 when the energy conversion efficiency η is assumed 85%. Therefore, the frame type of EE100 is selected, and turn ratios of n_D and n_H as well as N_1 turns of primary side are computed as follows:

$$n_D = \frac{N_{2D}}{N_1} = \frac{V_D/4}{\frac{2V_{\rm bus}}{\pi}\sqrt{1-\cos(2\pi D_c)}} \tag{2}$$

$$n_H = \frac{N_{2H}}{N_1} = \frac{v_H}{\frac{2V_{\rm bus}}{\pi}\sqrt{1-\cos(2\pi D_c)}} \tag{3}$$

$$N_1 = \frac{\frac{2V_{bus}}{\pi}\sqrt{1-\cos(2\pi D_c)}}{A_e \cdot \Delta B \cdot f_{sD,\min}}. \tag{4}$$

By using (2)–(4), n_D, n_H, and N_1 of 3.573, 0.103, and 55 are calculated with the selection of duty cycle D_c of 0.49. This is followed by the computation of N_{2D} of 197 turns and N_{2H} of 18 turns. Subsequently, the root-mean-square values of $i_{p,rms}$, I_D, and $i_{H,rms}$ of 6.541 $A_{\rm rms}$, 0.275 A, and 5 $A_{\rm rms}$ are obtained by using the following equations:

$$i_{p,\rm rms} = \frac{(P_D + P_H)/\eta}{\frac{\sqrt{2}V_{\rm bus}}{\pi}\sqrt{1-\cos(2\pi D_c)}} \tag{5}$$

$$I_D = P_D/V_D \text{ and } i_{H,\rm rms} = P_H/v_{H,\rm rms}. \tag{6}$$

At this time, the winding areas of A_{wp}, A_{wD}, and A_{wH} of 1.635, 0.069, and 1.25 mm^2 are accordingly calculated. Diameters of d_{wp}, d_{wD}, d_{wH} of 1.443, 0.296, and 1.262 mm are obtained. According to UEW Class 0 standard, this article selects the copper conductor for the primary and secondary side and diameters of 1.5, 0.3, and 1.3 mm are chosen for the winding of N_1, N_{2D}, and N_{2H}, respectively. Table II summarize these design results.

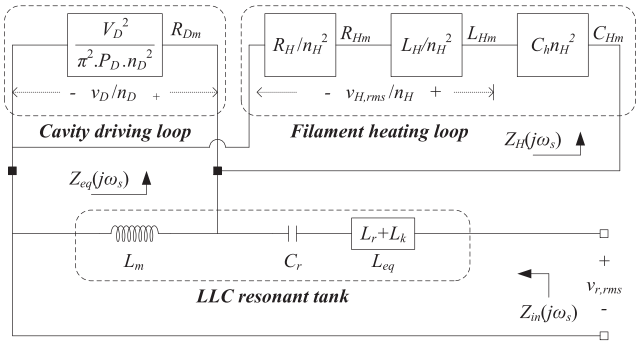

Fig. 3. Simplified architecture of the resonant power circuit.

III. Analysis of Resonant Power Circuits

Fig. 3 depicts the simplified resonant power circuit, where $v_{r,rms}$ represents the root-mean-square value of square-wave voltage of inverter output, and R_{Dm} represents the cavity load mapped to the primary side based on the turn ratio of n_{2D}. It is worth mentioning that R_{Dm} can be deemed as the nonoscillating equivalence resistance of R_s before driving or the oscillating equivalence resistance of D_z, R_z, and V_z after driving. The circuit of Fig. 3 resembles the *LLC* resonant one, where the quality factor of Q_{LLC} varies with the change of load R_{Dm} or R_{Hm}. If Q_{LLC} increases, then the circuit exhibits series resonance and the voltage gain becomes smaller than unity, making it suitable for voltage step-down. However, if Q_{LLC} decreases, then the circuit presents the series–parallel resonance feature, where the voltage gain is larger than one and suitable for voltage boosting. The series resonance frequency $f_{r,s}$ and the series–parallel resonance frequency $f_{r,sp}$ of *LLC* tank are expressed as follows:

$$f_{r,s} = \frac{1}{2\pi\sqrt{L_{\rm eq}C_r}} \text{ and } f_{r,\rm sp} = \frac{1}{2\pi\sqrt{(L_{\rm eq}+L_m)C_r}} \quad (7)$$

where $L_{\rm eq}$ is the summation of L_r and L_k. When the circuit exhibits series–parallel resonance characteristics, it is helpful for cavity driving. When the circuit is operated at the series resonance condition, then it is suitable for filament heating. Therefore, by justifying the resonance frequency points of $f_{r,s}$ and $f_{r,sp}$ along with the adjustment of voltage transfer characteristics, it facilitates the comprehension of the operating mode of magnetron cavity driving and filament heating.

A. Resonant Gain Analysis for Cavity-Driving Loop

The cavity-driving loop of integrated resonant circuit is applied here to increase the voltage step-up ratio. Through the adjustment of $L_{\rm eq}$ and C_r of *LLC* tank, it ensures that the system induces the output dc voltage V_D of 4 kV for cavity. The transfer function G_{vD} of cavity-driving loop is written as follows:

$$G_{vD}(j\omega_s) = \left|\frac{v_D}{v_{r,\rm rms}}\right| = \frac{(j\omega_s L_m \parallel R_{Dm} \parallel Z_H(j\omega_s))\cdot n_D}{j\omega_s L_{\rm eq} + \frac{1}{j\omega_s C_r} + (j\omega_s L_m \parallel R_{Dm} \parallel Z_H(j\omega_s))}. \quad (8)$$

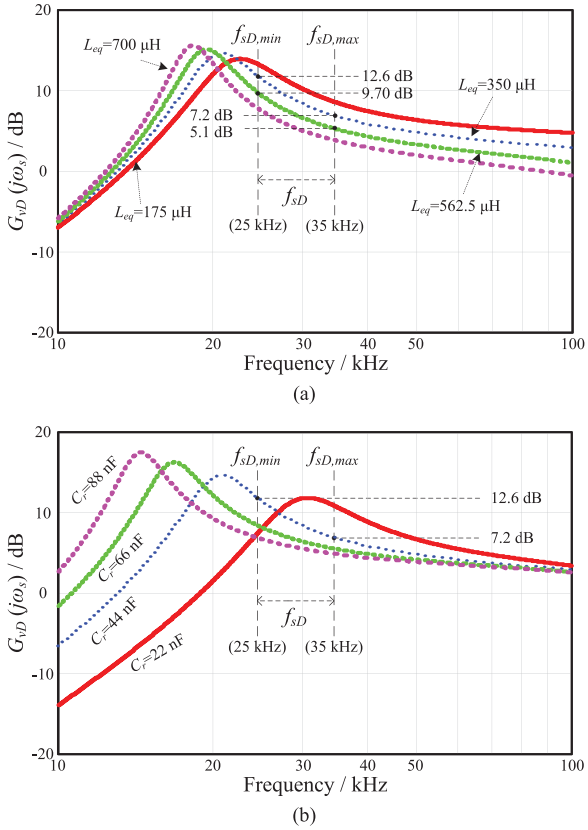

Fig. 4. Simulation results of voltage gain G_{vD} as a function of frequency under different (a) $L_{\rm eq}$ and (b) C_r conditions.

First, by selecting the series resonance frequency $f_{r,s}$ of 40 kHz for heating loop as well as the series–parallel frequency $f_{r,sp}$ of 20 kHz for driving loop, C_r is calculated to be 44 nF when $L_{\rm eq}$ equals 350 μH. Then, following the determination of voltage gain for stabilizing V_D, the suitable values of $L_{\rm eq}$ and C_r are evaluated.

Fig. 4 shows the simulation results of transfer gain G_{vD} under different values of $L_{\rm eq}$ and C_r (0.5, 1.0, 1.5, and 2.0 times) along with a 20% tolerance. The curve indicates that the frequency of f_{sD} ranging from 25 kHz ($f_{sD,min}$) to 35 kHz ($f_{sD,max}$) is suitable for cavity driving. In Fig. 4(a), through the adjustment of $L_{\rm eq}$ while maintaining C_r as 44 nF, the curve with $L_{\rm eq}$ of 350 μH indicates the sufficient voltage gain of 12.6 dB at $f_{sD,min}$ of 25 kHz as well as that of 7.2 dB at $f_{sD,max}$ of 35 kHz is reached. Therefore, the curve with C_r of 44 nF as shown in Fig. 4(b) demonstrates a linear variation of resonance gain and realizes the constant-power operation, illuminating the effective regulation of driving power. Moreover, as seen from the right-hand side of 35 kHz in Fig. 4(a), the voltage gain of cavity-driving loop decreases when the frequency increases. This feature facilitates the emission of thermal electron of filament electrode, assisting in the heating process with a low driving voltage.

B. Resonant Gain Analysis for Filament-Heating Loop

The filament-heating loop of resonant power circuit is designed to reduce the voltage ratio. By way of $L_{\rm eq}C_r$ series

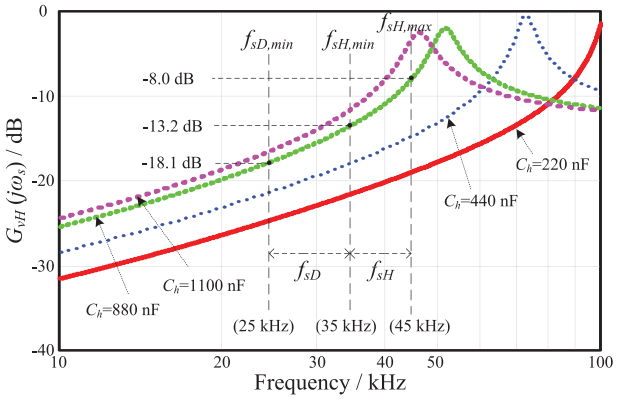

Fig. 5. Simulation curves of voltage transfer gain G_{vH} with different C_h.

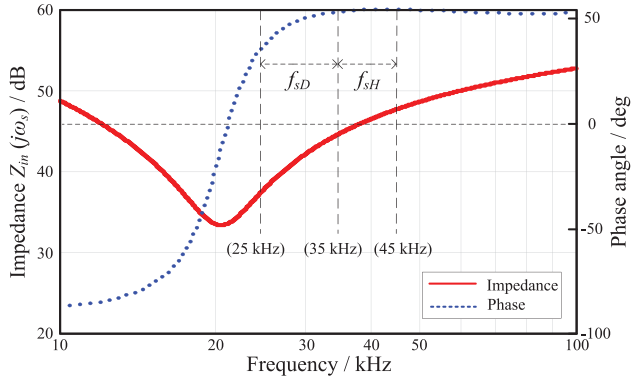

Fig. 6. Simulation curves of total input impedance Z_{in} and phase angle.

TABLE III
PARAMETERS OF RESONANT POWER CIRCUIT

Specifications	Symbols	Values
Equivalent resonance inductance	L_{eq}	350 μH
Capacitance of *LLC* resonance tank	C_r	44 nF
Series resonance capacitance	C_h	880 nF

resonance in an *LLC* resonant tank as well as $L_H C_h$ series resonance of filament, the circuit delivers the low heating voltage of v_H and large heating current of i_H to filament and cathode terminal. This voltage transfer function G_{vH} of heating loop is derived as follows:

$$G_{vH}(j\omega_s) = \left|\frac{v_{H,\text{rms}}}{v_{r,\text{rms}}}\right| = \frac{(j\omega_s L_{Hm}+R_{Hm})}{\left(\frac{1}{j\omega_s C_{Hm}}+j\omega_s L_{Hm}+R_{Hm}\right)} \cdot \frac{(j\omega_s L_m \| R_{Dm} \| Z_H(j\omega_s)) \cdot n_H}{j(\omega_s L_{\text{eq}} - \frac{1}{\omega_s C_r}) + (j\omega_s L_m \| R_{Dm} \| Z_H(j\omega_s))}. \quad (9)$$

Fig. 5 illustrates the simulation curves in which both L_{eq} of 350 μH and C_r of 44 nF are selected based on the above discussion. In this figure, for the gain curve with C_h of 880 nF, the voltage gain is -8.0 dB at $f_{sH,max}$ of 45 kHz and -13.2 dB at $f_{sH,min}$ of 35 kHz. Based on the selection of these parameters by use of microcontroller unit (MCU), the initial filament heating (operated at $f_{sH,max}$ of 45 kHz) and low-current continuous heating to induce electron emission for constant heat generation (operated at $f_{sH,min}$ of 35 kHz) can be both realized.

Next, when the system is operated at cavity-driving mode within the operable range of f_{sD}, the voltage gain of G_{vH} becomes -18.1 dB at 25 kHz, which is good at reducing the heating current to avoid disturbing the operating voltage V_D of the cavity. The gain of G_{vH} is, meanwhile, sufficient to induce the heating current of i_H continuously without extra preheating current loss. This gain value of G_{vH} can be also flexibly adjusted to decrease the heating current or shut down the operation, hence reducing the noise interference to the cavity. Table III lists the parameters of resonant circuit for this article.

C. Input Impedance and Phase Characteristics

The section is aimed at analyzing the input impedance Z_{in} and phase characteristics of the resonant circuit of Fig. 3, validating the merit of switching loss reduction. The input impedance Z_{in} of the resonant circuit is expressed as

$$Z_{\text{in}}(j\omega_s) = j\left(\frac{\omega_s^2 L_{\text{eq}} C_r - 1}{\omega_s C_r}\right) + (j\omega_s L_m \parallel R_{Dm} \parallel Z_H(j\omega_s)). \quad (10)$$

Fig. 6 delineates the relation between the input impedance Z_{in} and phase of the integrated resonant circuit. The inductive feature is observed when the system is operated at the right-hand side of 25 kHz ($f_{sD,min}$), and the zero-voltage switching of MOSFETs is realized. This curve implies that the lower operating frequency would result in smaller impedance, forming a larger driving current of I_D. The smooth variation of linear impedance ranging from 25 to 35 kHz further ensures an achievement of constant-power operation for magnetron drive.

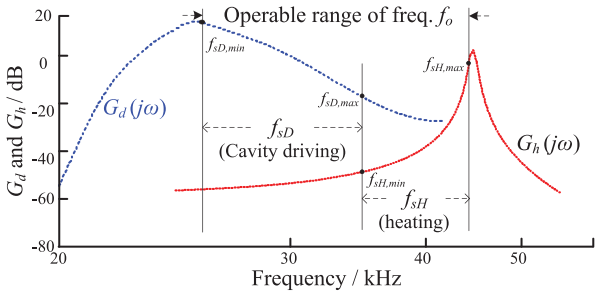

Fig. 7. Gain-frequency regulation of filament-heating and cavity-driving resonance.

IV. CONTROL OF GAIN-FREQUENCY REGULATION

By combining the filament-heating loop with cavity-driven loop as a single-stage circuit, this article goes to investigate the gain-frequency regulation control for magnetrons. Fig. 7 illustrates the gain-frequency curves of both heating (G_h) and driving (G_d) resonances. The figure indicates that the frequency of f_{sD} and f_{sH} ranges from 25–35 kHz to 35–45 kHz. In the figure, the low-gain curve of G_h is used to reduce the voltage ratio of v_H for filament heating, and the high-gain curve of G_d is to increase the voltage ratio of V_D for cavity driving. The system initializes with MCU starting at f_o of 45 kHz ($f_{sH,max}$) for high current of i_H to speed up the heating. This is followed by the tuning of f_o from $f_{sH,max}$ to $f_{sH,min}$ for the regulation control of

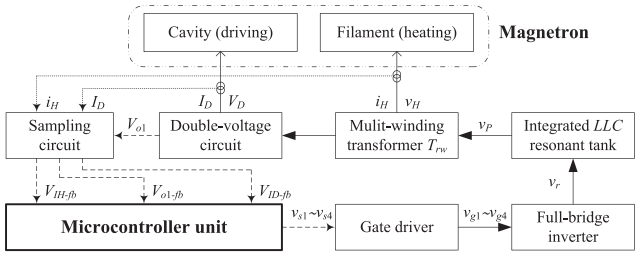

Fig. 8. Block diagram of gain-frequency control.

G_h, hence decreasing the heating current of i_H gradually. Only when the filament heating is finished, the system will operate at cavity-driving mode. At this time, f_o is operated between $f_{sD,max}$ and $f_{sD,min}$ so that the voltage gain of G_d can be better maintained. This way of gain-frequency regulation provides a systematic way of adjusting the operating voltage V_D and current I_D of the cavity, achieving the goal of constant-power control.

Fig. 8 depicts the block diagram of gain-frequency control method. In this figure, the MCU (PIC24FJ256GB106, Microchip) includes timer module, analog-to-digital converter, interrupt control, and output comparator. The sampling circuit is responsible for acquiring the heating current i_H, the capacitor voltage V_{o1} of double-voltage circuit, and the driving current I_D. Following the signals of i_H, I_D, and V_{o1} converted to voltage signals of $V_{IH\text{-}fb}$, $V_{ID\text{-}fb}$, and $V_{o1\text{-}fb}$, they are delivered to the MCU to perform the filament heating and constant-power control of gating driver. The driving power of P_D of the cavity is grasped based on the measured V_{o1} and I_D, where i_H is applied to ensure a continuous electron emission from the filament cathode. Note that through the adjustment of operating frequency f_o ranging from f_{sH} to f_{sD}, the amplitude of V_D and i_H can be effectively tuned. Distinctive features of this gain-frequency regulation control for magnetron drive includes: 1) the active adjustment of operating frequency to preheat the filament and then drive the cavity; 2) the extension to a wider range of operating frequencies for voltage modulation; and 3) the achievement of constant-power control for microwave stability.

Fig. 9 shows the flowchart of regulation control that consists of heating control mode and cavity-driving mode. When the system is activated, the controller is initialized and operated at the heating mode. The operating frequency of inverter starts at 45 kHz, by which the system delivers power to provide the heating current i_H and convert it to the direct current signal of V_{IH-fb}. The signal of V_{IH-fb} is then compared with that of V_{IH-ref}. If $V_{IH-fb} > V_{IH-ref}$, then the switching frequency of f_{sH} is deducted from $k_H|E_H|$, where E_H represents the error between feedback voltage of V_{IH-fb} and reference voltage of V_{IH-ref}, and k_H is the current multiplication ratio. In this way of voltage comparison, the system error can be reduced while the transient response is accelerated. Yet, if $V_{IH-fb} < V_{IH-ref}$, then f_{sH} and $k_H|E_H|$ are added to increases the output current i_H and speed up the filament heating. Once V_{IH-fb} equals V_{IH-ref}, then the timer module is activated. Only when the counting time of T_c amounts to the predetermined timer of $T_{\rm ref}$,

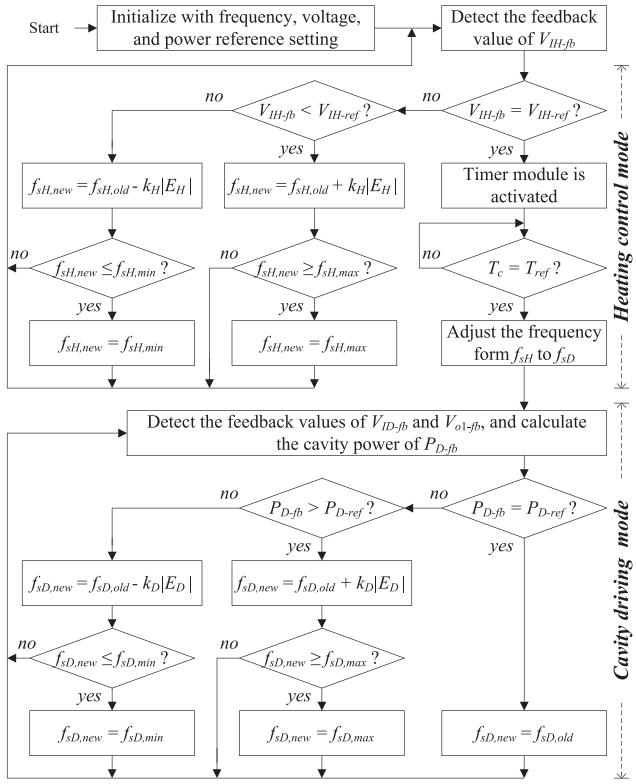

Fig. 9. Flowchart of the proposed gain-frequency regulation control.

the operating frequency of the inverter becomes f_{sD} while MCU is operated at cavity-driving mode.

Next, following the acquisition of dc feedback voltages of $V_{o1\text{-}fb}$ and V_{ID-fb}, the cavity-driving power P_{D-fb} is calculated and compared with the reference power P_{D-ref}. If $P_{D-fb} < P_{D-ref}$, then f_{sD} and $k_D|E_D|$ are deducted, where E_D denotes the error between P_{D-fb} and P_{D-ref}, and k_D denotes the gain coefficient; yet, if $P_{D-fb} > P_{D-ref}$, then f_{sD} is added to $k_D|E_D|$. The switching frequency range of f_{sH} and f_{sD} of this article are 45 kHz ($f_{sH,max}$) down to 35 kHz ($f_{sH,min}$) and 35 kHz ($f_{sD,max}$) down to 25 kHz ($f_{sD,min}$), respectively. It is worth mentioning that parameters of frequencies of $f_{sH,max}$, $f_{sH,min}$, $f_{sD,max}$, and $f_{sD,min}$ can be flexibly selected based on the specification of the magnetron. Meanwhile, the control mechanism can be designed to tune the current multiplication ratio k_H of heating control as well as the gain coefficient k_D of cavity-driven control so as to decrease the operation error of $k_H|E_H|$ and $k_D|E_D|$, hence improving the stability of filament heating and cavity operation. After the aforementioned control, the design of magnetron-driven system with feedback control is completed. Hardware realization along with its experimental results will be detailed in the next section.

V. Experimental Results

To validate the feasibility of the proposed system for magnetron drive, a hardware circuit is constructed. The high-voltage probe (P6015A, Tektronix), high-voltage differential probe

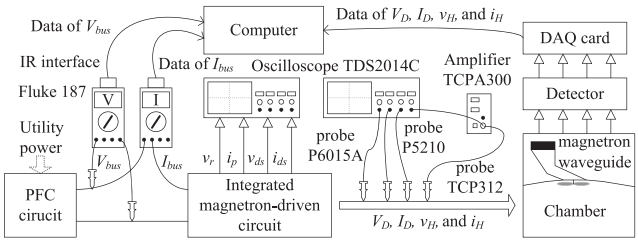

Fig. 10. Block diagram of the test setup.

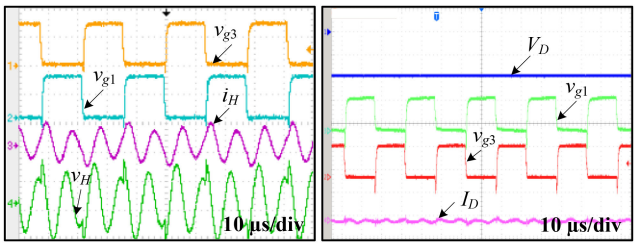

Fig. 11. Measured waveforms with (a) filament-heating operation and (b) cavity-driving operation. (v_H: 60 V/div, i_H: 20 A/div, V_D: 2 kV/div, I_D: 500 mA/div, v_{g1}: 10 V/div, and v_{g3}: 10 V/div.)

(P5210, Tektronix), and current probe (TCP312, Tektronix) with an amplifier (TCPA300, Tektronix) are employed to measure the magnetron voltage and current. Fig. 10 shows the block diagram of the test setup that consists of power factor-correction (PFC) circuit, integrated magnetron-driven circuit, chamber, detector, data-acquisition (DAQ) card, and personal computer. The data collected through the DAQ card along with the data received from the probe are sent to the computer for the test analysis. The 5-Ω and 16-kΩ resistors serve as the dummy load individually for heating and driving loop, by which the voltage $V_{\rm bus}$ of 310 V is adopted. The power circuit reaches an efficiency of 93.1% with P_D of 1 kW. Then, the system efficiency of 87.2%, 88.4%, 89.9%, and 91.5% is also recorded when the operating power P_D is 0.2, 0.4, 0.6, and 0.8 kW with the corresponding operating frequency f_o of 29.65, 28.21, 26.98, 26.32, and 25.90 kHz, respectively.

A. *Integrated Resonant Power Circuit Test*

Fig. 11 shows the measured waveforms of v_H, i_H, V_D, and I_D. After the cathode filament heating of Fig. 11(a) with f_{sH} of 41.8 kHz, V_D and I_D are measured to be 29.7 $V_{\rm rms}$ and 14.3 $A_{\rm rms}$ as Fig. 11(b) delineates. These results support the feasibility of the method for filament heating (41.8 kHz) and cavity driving (32.6 kHz), validating the completion of gain-frequency regulation and operation current control. The sequential operation of this proposed approach for heating and driving is stable as well when compared with the previous published method [6].

Fig. 12 shows the measured waveforms of phase angle θ between v_r and i_p under various operating conditions. In Fig. 12(a), the phase angle θ is 54° when the cavity is initially operated at 200 W. By adjusting the operating power of cavity to be 400, 600, and 800 W, the phase angle θ becomes 43°, 35°, and 27°, respectively. These results reveal that the resonant circuit can be operated at inductive feature, exhibiting the practicality of the resonant tank for magnetron drive.

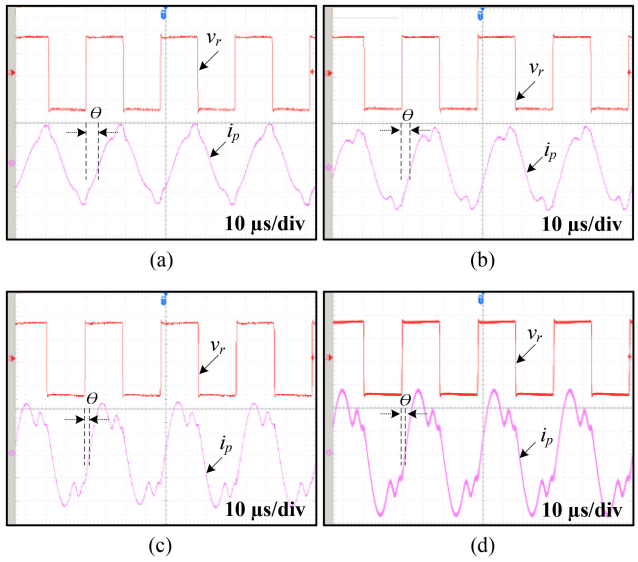

Fig. 12. Measured waveforms of v_r and i_p with the operating power of (a) 200 W, (b) 400 W, (c) 600 W, and (d) 800 W. (v_r: 200 V/div, i_p: 20 A/div.).

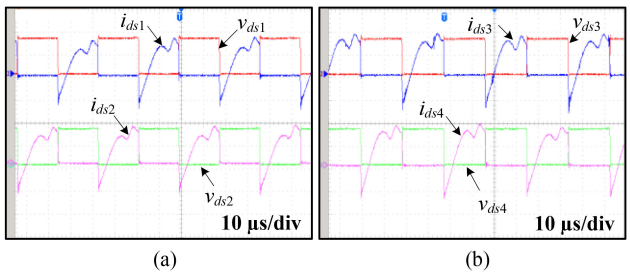

Fig. 13. Waveforms of (a) MOSFETs (T_1 and T_2) and (b) MOSFETS (T_3 and T_4) when the circuit reaches zero-voltage switching and P_D is operated at 200 W. (V_{ds1}–V_{ds4}: 200 V/div, I_{ds}–I_{ds4}: 2 A/div.).

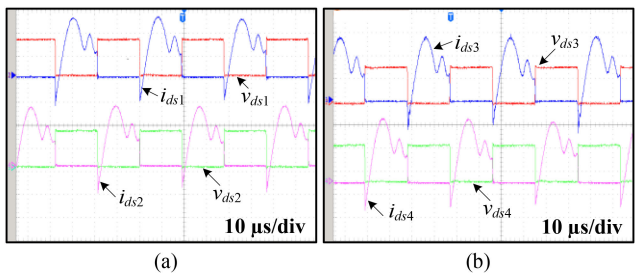

Fig. 14. Waveforms of (a) MOSFETs (T_1 and T_2) and (b) MOSFETS (T_3 and T_4) when the circuit reaches zero-voltage switching and P_D is operated at 1 kW. (V_{ds1}–V_{ds4}: 200 V/div, I_{ds}–I_{ds4}: 2 A/div.).

Following the confirmed inductive features of Fig. 12, Figs. 13 and 14 depict the waveforms of voltage (v_{ds1}–v_{ds4}) and current (i_{ds1}–i_{ds4}) of MOSFETs T_1–T_4 as shown in Fig. 1, where P_D is individually operated at light load of 200 W and heavy load

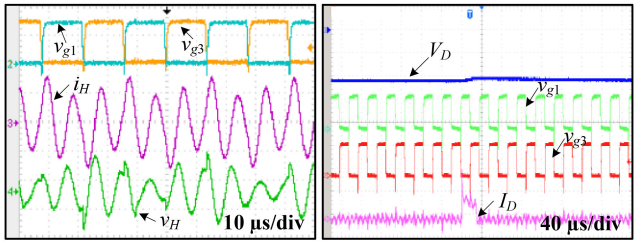

Fig. 15. Experimental results of (a) filament heating and (b) cavity driving under power P_D of 200 W. (v_H: 40 V/div, i_H: 10 A/div, V_D: 2 kV/div, I_D: 500 mA/div, v_{g1}: 10 V/div, and v_{g3}: 10 V/div.).

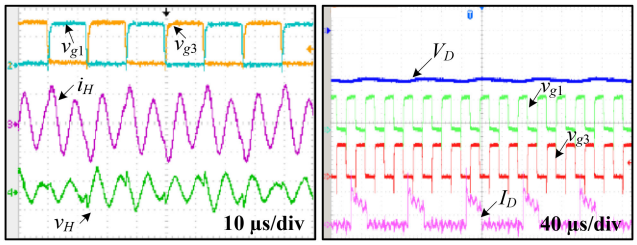

Fig. 16. Experimental results of (a) filament heating and (b) cavity driving under power P_D of 600 W. (v_H: 40 V/div, i_H: 10 A/div, V_D: 2 kV/div, I_D: 500 mA/div, v_{g1}: 10 V/div, and v_{g3}: 10 V/div.).

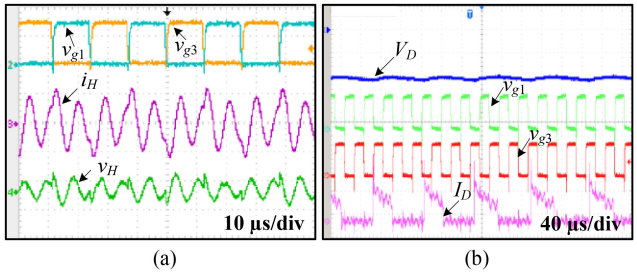

Fig. 17. Experimental results of (a) filament heating and (b) cavity driving under power P_D of 1 kW. (v_H: 40 V/div, i_H: 10 A/div, V_D: 2 kV/div, I_D: 500 mA/div, v_{g1}: 10 V/div, and v_{g3}: 10 V/div.).

of 1 kW. In these figures, when those waveforms of v_{ds1}–v_{ds4} are measured at low level because T_1–T_4 are turned ON, the negative current waveforms of i_{ds1}–i_{ds4} are simultaneously observed. This observation reveals that the currents of i_{ds1}–i_{ds4} run through the body diode of MOSFETs (SCT2080KE, Rohm). The zero-voltage switching is achieved, benefiting the reduction of switching loss.

B. Gain-Frequency Regulation Control Test

Figs. 15–17 depict the measured results of cavity driving with constant-power control under different operating conditions. V_D and I_D are controlled through the tracking of voltage transfer gain of G_{sD} so as to ensure that the cavity power of P_D is well maintained. In Fig. 15, when the driving power P_D is 200 W, f_o, V_D, and I_D are 29.77 kHz, 4.19 kV, and 49.59 mA, respectively. Then, in Fig. 16, f_o, V_D, and I_D becomes 27.11 kHz, 4.114 kV, and 149.6 mA when P_D is operated at 600 W. Next, when P_D amounts to 1 kW, the curves of Fig. 17 indicate that f_o, V_D, and I_D are 26.12 kHz, 3.963 kV, and 254.1 mA. These waveforms solidify the capability of constant-power control of the proposed system.

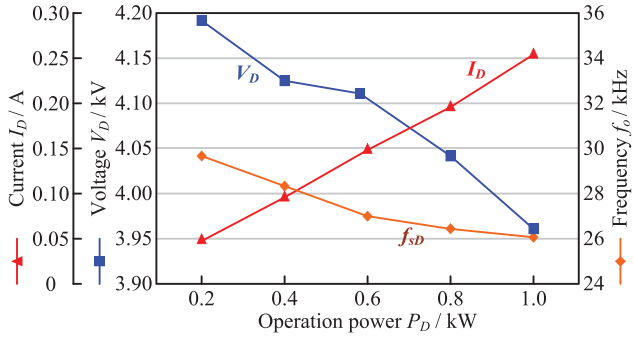

Fig. 18. Measured results of operating frequency f_{sD}, voltage V_D, and current I_D obtained under different operating power.

TABLE IV
MEASURED RESULTS OF MAGNETRON DRIVE

P_D (w)	f_o (kHz)	V_D (kV)	I_D (mA)	v_H (V_{rms})	i_H (A_{rms})
200	29.77	4.190	49.59	21.7	8.80
400	28.36	4.127	98.12	16.7	8.02
600	27.11	4.114	149.6	13.8	7.28
800	26.69	4.043	197.7	12.6	6.84
1000	26.12	3.963	254.1	11.3	5.95

Fig. 18 shows the operation frequency f_o, voltage V_D, and current I_D under various cavity-driving power P_D. Table IV lists the experimental results of driving and heating for this test. When the operating power P_D of the cavity is increased from 0.2 to 1.0 kW, its operating frequency f_o is gradually adjusted from 29.77 kHz down to 26.12 kHz with the aid of gain-frequency regulation control. As an example, with the operating power of 400 W increased to 800 W, f_{sD}, V_D, and I_D vary from 28.4 kHz, 4.125 kV, and 93.12 mA to 26.44 kHz, 4.043 kV, and 194.8 mA. These measurements confirm the frequency-tracking operation, which also indicates that the current grows when the voltage of V_D drops following the increased operating power, hence demonstrating the negative impedance feature.

To better comprehend the microwave output power P_M, the IEC60705 is referred here for the calculation of microwave output power, by which the microwave power P_M is computed based on the temperature rise of one-minute water heating. The results indicate that the microwave output power P_M is 0.139, 0.289, 0.445, 0.611, and 0.789 kW after one-minute heating when P_D is operated at 0.2, 0.4, 0.6, 0.8, and 1.0 kW, respectively. The conversion efficiency of microwave output from P_D to P_M is about 69.5%–78.9%, which is related with antenna loss of cavity, waveguide loss, and space environment of chamber.

Fig. 19 shows the operating curves of magnetron cavity with and without gain-frequency tracking control mechanism. As depicted in the figure, when the cavity is operated without constant-power control, an unstable condition is observed, as the

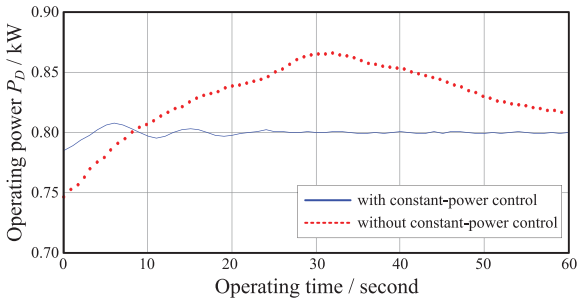

Fig. 19. Measured results of operating power P_D obtained with and without constant-power control mechanism.

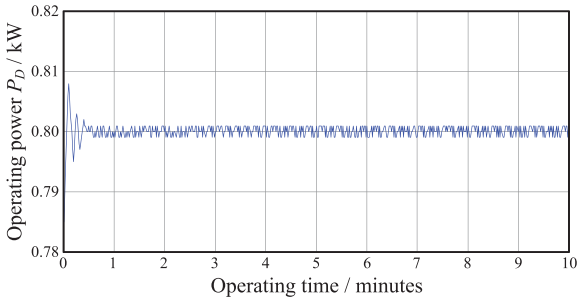

Fig. 20. Output power P_D obtained with constant-power control during 10 min operation.

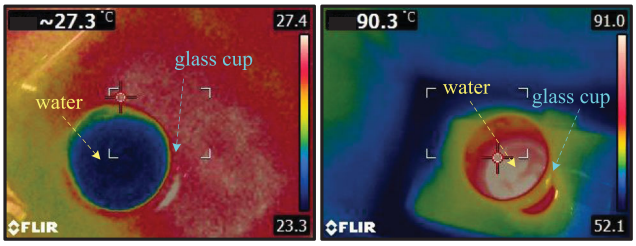

(a) (b)

Fig. 21. Photograph of a real load operated (a) without magnetron-driven heating and (b) with magnetron-driven heating after 30 s.

red dot indicates. Then, following the employment of constant-power control through an effective parameter tuning of heating control as well as cavity-driven control, the microwave output is seen to be maintained at 800 W of higher stability.

Fig. 20 shows the operating power curves of magnetron cavity for the duration of 10 min under gain-frequency tracking control. The curve indicates that the cavity achieves constant-power operation after the first 29-s driving, where the subsequent operating power comes with only ±3 W deviation, supporting the advantage of the proposed control method.

Fig. 21 is the photograph of a real load (a glass cup of water) operated with and without the proposed magnetron-driven system. The infrared camera (FLIR-E5) is employed to measure the thermal image of this load. In Fig. 21(a), the temperature is measured to be 27.3 °C. Then, in Fig. 21(b), by activating the magnetron oscillation for 30 s, the load temperature rises to 90.3 °C. At this time, the surface temperature is evenly distributed, assisting in the emission of microwave energy to increase the heating temperature swiftly. By comparing the proposed method with the previously reported approach [6], the distinctive features of this article lie in: 1) the realization of constant-power control which is less affected by the variation of magnetron impedance; 2) the combination of heating loop and driving loop as a single-stage power circuit; and 3) the achievement of gain-frequency regulation control with filament heating first and cavity driving next. Experiences gained from these practical tests may serve useful references for microwave industry applications.

VI. Conclusion

This article presents an integrated single-stage resonant power circuit and gain-frequency regulation mechanism for a magnetron-driven system. Resonant analysis and operation frequency characteristics are individually made for magnetron cavity-driving loop and filament-heating loop, which accompanies with the investigation of circuit parameters and multi-winding transformer design. The proposed method effectively performs filament heating and cavity driving with constant-power control, where the zero-voltage switching is meanwhile achieved. Experimental outcomes validate the practicality of the proposed circuit and control method, benefiting electric power applications of magnetron systems.

References

[1] R. Scapaticci, P. Kosmas, and L. Crocco, "Wavelet-based regularization for robust microwave imaging in medical applications," *IEEE Trans. Biomed. Eng.*, vol. 62, no. 4, pp. 1195–1202, Apr. 2015.

[2] R. K. Verma, S. Maurya, and V. V. P. Singh, "Study of mode control in long-anode high-power pulse magnetron," *IEEE Trans. Plasma Sci.*, vol. 42, no. 12, pp. 4010–4014, Dec. 2014.

[3] A. Sayapin, U. Dai, and Y. E. Krasik, "S-band relativistic magnetron operation with multichannel radial outputs of the microwave power," *IEEE Trans. Plasma Sci.*, vol. 45, no. 2, pp. 229–234, Feb. 2017.

[4] M. A. Franzi *et al.*, "Recirculating-planar-magnetron simulations and experiment," *IEEE Trans. Plasma Sci.*, vol. 41, no. 4, pp. 639–645, Apr. 2013.

[5] M. A. Franzi *et al.*, "Microwave power and phase measurements on a recirculating planar magnetron," *IEEE Trans. Plasma Sci.*, vol. 43, no. 5, pp. 1675–1682, May 2015.

[6] D. Martin, A. Jianu, and D. Ighigeanu, "A method for the 2.45-GHz magnetron output power control," *IEEE Trans. Microw. Theory Techn.*, vol. 49, no. 3, pp. 542–545, Mar. 2001.

[7] Y. J. Woo, M. C. Lee, K. C. Lee, and G. H. Cho, "One-chip class-E inverter controller for driving a magnetron," *IEEE Trans. Ind. Electron.*, vol. 56, no. 2, pp. 400–407, Feb. 2009.

[8] Y. J. Woo, S. K. Kim, and G. H. Cho, "Voltage-clamped class-E inverter with harmonic turning network for magnetron drive," *IEEE Trans. Circuits Syst. II, Express Briefs*, vol. 53, no. 12, pp. 1456–1460, Dec. 2006.

[9] I. Tahir, A. Dexter, and R. Carter, "Noise performance of frequency- and phase-locked CW magnetrons operated as current-controlled oscillators," *IEEE Trans. Electron Devices*, vol. 52, no. 9, pp. 2096–2103, Sep. 2005.

[10] H. L. Bosman, M. I. Fuks, S. Prasad, and E. Schamiloglu, "Improvement of the output characteristics of magnetrons using the transparent cathode," *IEEE Trans. Plasma Sci.*, vol. 34, no. 3, pp. 606–619, Jun. 2006.

[11] S. R. Jang, H. J. Ryoo, S. H. Ahn, J. S. Kim, and G. H. Rim, "Development and optimization of high-voltage power supply system for industrial magnetron," *IEEE Trans. Ind. Electron.*, vol. 59, no. 3, pp. 1453–1461, Mar. 2012.

[12] M. J. Kim, W. S. Choi, I. W. Jeong, H. C. Park, and K. H. Park, "A new driving method of the magnetron power supply for a sulfur plasma lamp," *IEEE Trans. Ind. Electron.*, vol. 63, no. 9, pp. 5416–5424, Sep. 2016.

[13] D. G. Bandeira, T. Brunelli, and I. Barbi, "High voltage power supply using a T-type parallel resonant DC-DC converter," *IEEE Trans. Ind. Appl.*, vol. 54, no. 3, pp. 2459–2470, Jan./Feb. 2018.
[14] J. M. Alonso, J. García, A. J. Calleja, J. Ribas, and J. Cardesín, "Analysis, design, and experimentation of a high-voltage power supply for ozone generation based on current-fed parallel-resonant push-pull inverter," *IEEE Trans. Ind. Appl.*, vol. 41, no. 5, pp. 1364–1372, Sep. /Oct. 2005.
[15] S. Chudjuarjeen, A. Sangswang, and C. Koompai, "An improved LLC resonant inverter for induction-heating applications with asymmetrical control," *IEEE Trans. Ind. Electron.*, vol. 58, no. 7, pp. 2915–2925, Jul. 2011.
[16] J. W. Kim, M. H. Park, B. H. Lee, and J. S. Lai, "Analysis and design of LLC converter considering output voltage regulation under no-load condition," *IEEE Trans. Power Electron.*, vol. 35, no. 1, pp. 522–534, Jan. 2020.
[17] M. Li, Z. Ouyang, and M. A. E. Andersen, "High-frequency LLC resonant converter with magnetic shunt integrated planar transformer," *IEEE Trans. Power Electron.*, vol. 34, no. 3, pp. 2405–2415, May 2018.
[18] V. Kinnares and P. Hothongkham, "Circuit analysis and modeling of a phase-shifted pulsewidth modulation full-bridge-inverter-fed ozone generator with constant applied electrode voltage," *IEEE Trans. Power Electron.*, vol. 25, no. 7, pp. 1739–1752, Jul. 2010.
[19] T. Mishima, S. Sakamoto, and C. Ide, "ZVS phase-shift PWM-controlled single-stage boost full-bridge AC–AC converter for high-frequency induction heating applications," *IEEE Trans. Ind. Electron.*, vol. 64, no. 3, pp. 2054–2061, Mar. 2017.
[20] T. Mishima, C. Takami, and M. Nakaoka, "A new current phasor-controlled ZVS twin half-bridge high-frequency resonant inverter for induction heating," *IEEE Trans. Ind. Electron.*, vol. 61, no. 5, pp. 2531–2545, May 2014.
[21] H. Sarnago, Ó. Lucía, M. P. Tarragona, and J. M. Burdío, "Dual-output boost resonant full-bridge topology and its modulation strategies for high-performance induction heating applications," *IEEE Trans. Ind. Electron.*, vol. 63, no. 6, pp. 3554–3561, Jun. 2016.
[22] H. Ma, G. Chen, J. H. Yi, Q. W. Meng, L. Zhang, and J. P. Xu, "A single-stage PFM-APWM hybrid modulated soft-switched converter with low bus voltage for high-power LED lighting applications," *IEEE Trans. Ind. Electron.*, vol. 64, no. 7, pp. 5777–5788, Jul. 2017.
[23] V. Talla and J. R. Smith, "Design and analysis of a high bandwidth rectifying regulator with PWM and PFM modes," *IEEE Trans. Circuits Syst. II, Express Briefs*, vol. 63, no. 12, pp. 1121–1125, Dec. 2016.
[24] X. Sun, Y. Shen, W. Li, and H. Wu, "A PWM and PFM hybrid modulated three-port converter for a standalone PV/battery power system," *IEEE J. Emerg. Sel. Topics Power Electron.*, vol. 3, no. 4, pp. 984–1000, Dec. 2015.

Tsong-Shing Lee (Member, IEEE) received the Ph.D. degree in electrical engineering from National Cheng Kung University, Tainan, Taiwan, in 2015.

From 2004 to 2016, he was with AU Optronics Corporation, Hsinchu, Taiwan. Since 2016, he has been with the Department of Electrical Engineering, Southern Taiwan University of Science and Technology, Tainan, Taiwan, where he is currently an Associate Professor. His research interests include power electronic converters, inductively coupled power transfer systems, display power supply, resonant circuit, and piezoelectric transformer power application.

Shyh-Jier Huang (Senior Member, IEEE) received the Ph.D. degree in electrical engineering from the University of Washington, Seattle, WA, USA, in 1994.

He is a Distinguished Professor with the Department of Electrical Engineering, National Cheng Kung University, Tainan, Taiwan. His current research interests include electric power quality, power delivery, and signal-processing applications.

Dr. Huang was the recipient of the Outstanding Research Award from the National Science Council of Taiwan in 2004, and the Outstanding Technical Achievement Award from IEEE Tainan Section in 2016. He was the IEEE Taipei Chapter Chair of the IEEE Power Engineering Society from 2002 to 2003.

Yu-Ren Lin was born in Tainan, Taiwan, in 1993. He received the B.S. degree from the National Yunlin University of Science and Technology, Yunlin, Taiwan, in 2015, and the M.S. degree from National Cheng Kung University, Tainan, Taiwan, in 2017, both in electrical engineering.

He is with MediaTek, Inc., Hsinchu, Taiwan. His research interests include power electronics, wireless power transfer, and power management IC design.

Te-Chun Hung (Member, IEEE) received the Ph.D. degree in electrical engineering from National Cheng Kung University, Tainan, Taiwan, in 2016.

From 2013 to 2018, he was with Delta Electronics, Inc., Tainan, Taiwan. Since 2018, he has been with the Department of Electrical Engineering, Southern Taiwan University of Science and Technology, Tainan, Taiwan, where he is currently an Assistant Professor. His research interests include power electronics circuit design and power electronics applications.

Chien-Chang Chen (Member, IEEE) was born in Kaohsiung, Taiwan, in 1977. He received the M.S. and Ph.D. degrees in electrical engineering from National Cheng Kung University, Tainan, Taiwan, in 2007 and 2014, respectively.

He is currently an Assistant Professor with the Department of Automation Engineering, National Formosa University, Huwei, Taiwan. His research interests include electromagnetic measurement and control system, AI fast and precise calculation system, microwave and radio frequency application system, power electronics system, and bioelectronic instrumentation.